The effect of squeeze film constriction on bandwidth improvement in interferometric accelerometers

Maximillian A Perez and Andrei M Shkel

MicroSystems Laboratory, Mechanical and Aerospace Engineering Department,
University of California at Irvine, 4200 Engineering Gateway, Irvine, CA 92697, USA

E-mail: max.perez@uci.edu and andrei.shkel@uci.edu

Abstract
This paper studies the effects of a constricted squeeze film on the performance of an optical
microelectromechanical system accelerometer. Squeeze films are shown to extend the sensor
frequency range (bandwidth) in accelerometers without decreasing the mechanical sensitivity
by retarding the resonate response. By restricting the venting of a squeeze film, this
preferential behavior is observed at lower frequencies than is expected for ideally vented
accelerometers. Due to this effect, constricted squeeze films may be used to improve the
bandwidth performance of devices of lower natural frequencies and higher inertial
sensitivities. A model, extended from the existing squeeze film theory, is developed for the
squeeze film formed between circular plates with generalized mixed boundary pressure
conditions to describe the boundary flow resistance. These effects are experimentally observed
in a parallel plate Fabry–Pérot interferometric accelerometer through frequency response
characterization at mechanical resonance under pressure variation. The analytical results for
the constricted squeeze film are used to predict the performance gains due to the
frequency-dependent squeeze film parameters. These results are experimentally confirmed by
demonstrating improved bandwidth performance due to the constricted squeeze film.

(Some figures in this article are in colour only in the electronic version)

1. Introduction

Structural members, such as flexural suspension elements, are traditionally considered to define the overall stiffness of the proof-mass element in inertial sensors. In many microelectromechanical system (MEMS) based sensors, however, the stiffness due to a squeeze film may be a significant contribution to the total stiffness of the system. In contrast to the stiffness due to flexural suspension members, the squeeze film stiffness is strongly frequency dependant. In specific cases, this frequency dependence introduces a useful dynamic response that extends the vibration range without reducing the mechanical sensitivity. Structures with high resonant frequencies may be required to take advantage of these properties under ambient pressures. By restricting the venting of squeeze films in accelerometer design, these requirements are relaxed to devices of lower resonant frequencies and higher inertial sensitivities.

Squeeze films are formed between closely vibrating surfaces due to the dynamic encapsulation of viscous gases. The earliest description of isothermal squeeze films was by Crandell in 1918 [1] for circular plates in parallel motion and was restated by both Langlois in 1962 [2] and Blech in 1982 [3]. Squeeze films are commonly encountered in MEMS sensors and actuators due to the small dimensions and the frequent reliance on vibratory motion [4]. Most existing efforts have focused on the characterization and reduction of squeeze film damping levels due to its role in limiting the quality factor of resonant devices [5]. Also frequently examined is squeeze films characteristics under nontrivial device geometries, especially perforations often incorporated to facilitate fabrication or to reduce damping levels [6].

Less frequently examined is the effect of squeeze film stiffening on non-resonant sensors, such as micromachined accelerometers. Most prominently, Yang *et al* [7, 8] and Andrews *et al* [9] considered the effects of both the damping

and the stiffness of a squeeze film formed between the plates of a vibrating microstructure on its frequency response. Viejola *et al* [10] introduced advanced squeeze film models to accurately predict the response of a micro-accelerometer. All present the non-trivial effects of a squeeze film on the response of capacitive micromachined devices, including those due to the squeeze film stiffness. The general effects on the low pass frequency response of a resonator is considered in the review by Boa and Yang [11]. However, the specific effects of the increased stiffness due to a squeeze film on sensor performance are neglected.

The constriction of squeeze film venting was considered analytically for square plates by Darling *et al* [12]. Simplified models for squeeze films with venting resistance were presented by Viejola *et al* [13]. However, experimental characterization of a constricted squeeze film is absent in these publications.

In this work, a closed-form squeeze film model is derived for general boundary conditions for circular plates. This model is used to demonstrate how nearly the full frequency range up to the structural natural frequency may be used as sensing bandwidth for accelerometers with a constricted squeeze film (section 2). Squeeze films are studied experimentally in a passive accelerometer based on Fabry–Pérot interferometry with an unvented gap between the planer proof-mass plus suspension structure and reference plates. Optical detection is selected for the characterization due to its high sensitivity, and external vibration excitation is used to eliminate potential contribution to the system response from electrostatic or magnetic fields. The stiffness contribution due to the flexure suspension and the squeeze film are independently evaluated using resonate characterization under a vacuum. The experimental response and analytical model are used to extract the squeeze film constriction parameter (section 3). The complete model is then evaluated and the response over the operational frequency range is considered. Finally, the performance gains in the accelerometer due to the constricted squeeze film are evaluated (section 4).

2. Modeling

Many micromachined structures, including the passive proof-mass optical accelerometer based on Fabry–Pérot interferometry shown in figure 1, may be constructed without vertical holes or horizontal vents. Under excitation of the sensor frame, the proof mass will deflect relative to the reference plate forming a squeeze film between the plates. Elimination of venting features in the proof mass of micromachined accelerometers is generally desirable due to the increased mass per unit area. However, the absence of venting features requires special attention as it will restrict the flow from the squeeze film formed between the deflected proof-mass and reference plates. In this section, the behavior of a squeeze film under such constricted conditions is considered.
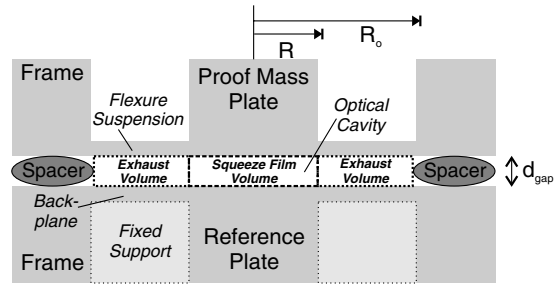
Figure 1. Cross-section of a Fabry–Pérot interferometric accelerometer with squeeze film constricted by a closed, unvented exhaust volume.
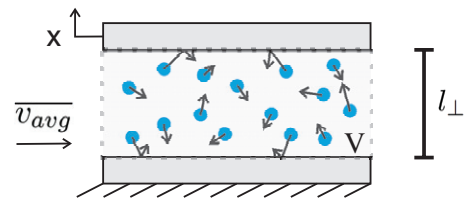
Figure 2. The discrete particles of the gas forming squeeze film, each with average velocity $\overline{v_{avg}}$ contained in a cavity between plates of perpendicular separation $l_\perp$ of volume V.

2.1. Gas rarefaction

Under reduced pressures, the effects of gas rarefaction on the behavior of a squeeze film has been shown to be characterized by the Knudsen number K_n, which is the ratio of the gas particle mean-free path to the plate gap separation d_{gap} [14]. For $K_n \ll 1$ the squeeze film is considered to be in the *continuous regime* and can be treated as a viscous fluid, to which this work is constrained [15]. Under conditions in which the Knudsen numbers approach 1, it becomes necessary to consider the reduction in the effective gas viscosity μ_{eff} from the gas viscosity μ due to the rarefication of the gas, which may be estimated in the first order by $\mu_{eff} = \mu/(1 + 6K_n)$ [13, 16]. Once Knudsen numbers greater than 1 are encountered, the energy gain in the squeeze film due to a momentum exchange between individual molecules and the vibrating plate element must be considered [15, 17]. This work is constrained to Knudsen numbers less than 1.

2.2. Simple compression spring

A simple model of the stiffness due to a squeeze film may be derived by modeling the enclosed gas particles as a completely constricted squeeze film of discrete particles, as in figure 2. The basic kinetic theory predicts the relation between the pressure on a surface and the kinetic energy of the surrounding gas particles. A well-known result for an enclosed volume (V) is that the force on one surface (F_s) of the volume is given by

$$F_s = \frac{N m_{gas} \overline{v_\perp^2}}{l_\perp},\tag{1}$$

where N is the number of particles in the volume, m_{gas} is the mass of each gas particle, $\overline{v_\perp}$ is the average velocity of the enclosed gas particles perpendicular to the surface
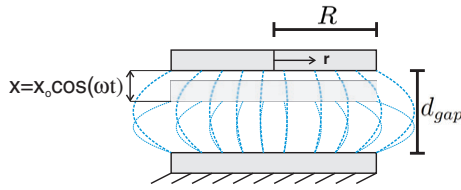
Figure 3. A continuous squeeze film formed between the fixed reference plate and the circular vibrating proof-mass plate with displacement x and radius R.

and $l_\perp$ is the dimension of the volume perpendicular to the surface [18].

Applying Hook's law $\left(k = -\frac{dF}{dx}\right)$, the stiffness of the enclosed volume (k_{vol}) under perpendicular (x) displacement of the plate is given as

$$k_{vol} = \frac{N m_{gas} \overline{v_\perp}^2}{l_\perp^2}. \tag{2}$$

Applying the ideal gas law ($P_a V = N k_B T$) and the velocity due to the thermal excitation of a particle $\left(\overline{v_\perp}^2 = k_B T / m_{gas}\right)$ to (2) yields

$$k_{sf,d} = \frac{P_a V}{l_\perp^2}, \tag{3}$$

which is the stiffness of a squeeze film ($k_{sf,d}$) due to simple compression of a gas in which the film can be considered as a simple *compression spring* under perpendicular displacement of the surfaces. As is frequently the most common case, for a volume contained by vibrating planer plates ($V = A l_\perp$), (3) reduces to

$$k_{sf,d} = \frac{P_a A}{l_\perp} = \frac{P_a A}{d_{gap}}, \tag{4}$$

where A is the area of the plate and d_{gap} is the gap spacing beneath the plate. This expression would be expected to be valid when the film gas is considered to be ideally contained between the plates, and ideal gas assumptions hold. Since it is assumed that the gas is fully contained, energy transferred from the plate to the gas will not be lost from the system and the damping in this model is zero.

2.3. Continuous squeeze film model

For a squeeze film in the continuous gas regime, the continuum behavior of the gas may be considered, as illustrated in figure 3. A more complete description of the squeeze film behavior, originally presented by Crandall [1], has been previously arrived at by solving the linearized compressible Reynolds gas-film problem [2, 3] represented in the form of the axisymmetric heat equation [19]. In this treatment, the in-phase and out-of-phase responses of the radial pressure distribution to sinusoidal displacement between circular plates is evaluated. This pressure distribution is then integrated over the plate surface to find the total resistance due to the squeeze film in terms of the stiffness (in-phase) and damping (out-of-phase) components. The solution is given in terms of the non-dimensional squeeze number σ, given for circular plates as

$$\sigma = \frac{12 \mu_{eff} R^2}{P_a d_{gap}^2} \omega, \tag{5}$$

where ω is the excitation frequency in radian, μ_{eff} is the effective gas viscosity and R is the plate radius.

2.3.1. Dirichlet boundary conditions. The expression for squeeze film stiffness was solved by Crandall assuming a homogenous Dirichlet (type one) boundary condition

$$[p(r) = 0]_{r=R} \tag{6}$$

at the outer edge of the squeeze film, where $p(r)$ is the total radial pressure distribution in excess of the ambient in the squeeze film. This assumes that an ideal pressure sink at the outer edge of the squeeze film allows the excess pressure to go to zero, which is referred to by Crandall as 'free communication with the atmosphere'. Adapted from the representation presented by Blech [3], the squeeze film stiffness for a circular plate is given by

$$k_{sf,c} = \left\{ 1 + \sqrt{\frac{2}{\sigma}} [A_c(ber_1\sqrt{\sigma} + bei_1\sqrt{\sigma}) \right.$$
$$\left. + B_c(ber_1\sqrt{\sigma} - bei_1\sqrt{\sigma})] \right\} \frac{P_a A}{d_{gap}}, \tag{7}$$

where

$$A_c = \frac{bei\sqrt{\sigma}}{ber^2\sqrt{\sigma} + bei^2\sqrt{\sigma}}, \qquad B_c = \frac{ber\sqrt{\sigma}}{ber^2\sqrt{\sigma} + bei^2\sqrt{\sigma}}.$$

The Kelvin functions (ber_γ, bei_γ) can be calculated by

$$ber_\gamma(x) + i bei_\gamma(x) = J_\gamma(x\, e^{3\pi i/4}), \tag{8}$$

where $J_\gamma()$ is a Bessel function of the first kind. There is a slight error in the formulation of the equation given by Blech in [3] corrected in equation (7) here through comparison with the original work done by Crandall [1]. It is noted by Andrews *et al* [9] that in the limit of large squeeze numbers, the squeeze film stiffness solutions for square plates given by Blech converge to

$$k_{sf,c}(\sigma \gg 1) = \frac{P_a A}{d_{gap}}, \tag{9}$$

which is identical to equation (4) obtained previously using the simple discrete model.

2.3.2. Mixed boundary conditions. A more generally applicable solution for the squeeze film stiffness is derived in this work by considering the homogenous mixed (type three) boundary condition

$$\left[\kappa \frac{\partial p(r)}{\partial n} + p(r) \right]_{r=R} = 0, \tag{10}$$

which introduces a flow constriction across the squeeze film boundary described by the parameter κ.

Starting from the general solution after applying symmetry arguments (adapted from equation (7) in [1])

$$p(r) - \frac{P_a x_o \cos(\omega t)}{d_{gap}}$$
$$= C[ber\sqrt{\sigma}\cos(\omega t + \Phi) - bei\sqrt{\sigma}\sin(\omega t + \Phi)], \tag{11}$$

where $x_o \cos(\omega t)$ is the plate displacement excitation of a squeeze film and C and Φ are now determined by the boundary condition of (10). Following Crandall's treatment by
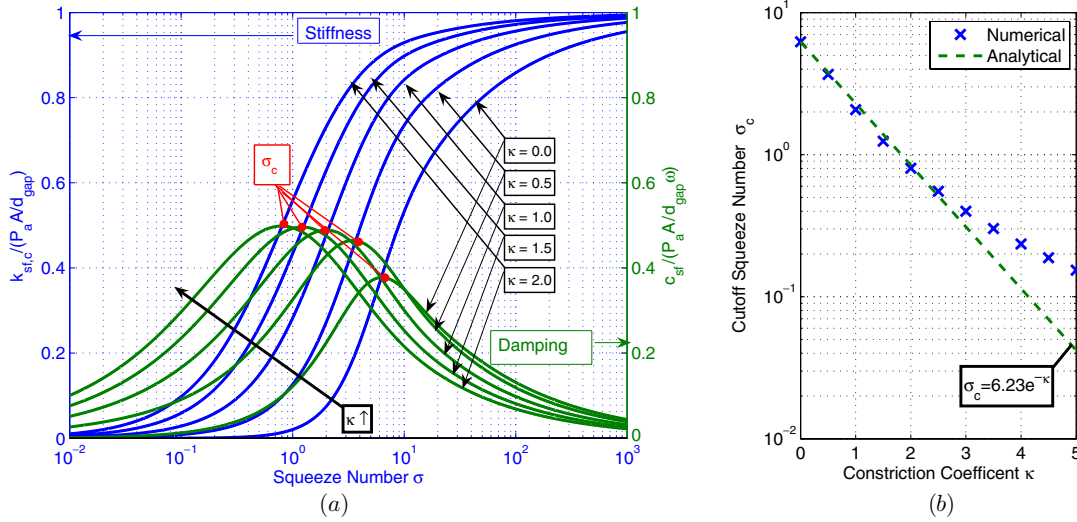
Figure 4. Variation of the (*a*) normalized squeeze film parameters and (*b*) cutoff squeeze number σ_c with the constriction coefficient κ.

considering only the in-phase component of the solution, $p_{\cos}$, which is in-phase with the plate displacement, and integrating the pressure distribution across the film according to

$$k_{\text{sf},c} = \frac{2\pi}{x_o \cos(\omega t)} \int_0^R p_{\cos} r \, \mathrm{d}r, \qquad (12)$$

which yields after extensive algebra the stiffness component of the squeeze film

$$k_{\text{sf},c} = \left\{ 1 + \sqrt{\frac{2}{\sigma}} [A_\kappa (ber_1 \sqrt{\sigma} + bei_1 \sqrt{\sigma}) \right. \qquad (13)$$
$$\left. + B_\kappa (ber_1 \sqrt{\sigma} - bei_1 \sqrt{\sigma})] \right\} \frac{P_a A}{d_{\text{gap}}},$$

where

$$A_\kappa = \frac{bei \sqrt{\sigma} + \frac{\sqrt{2}}{2} \kappa C_\kappa}{\left(ber \sqrt{\sigma} + \frac{\sqrt{2}}{2} \kappa D_\kappa\right)^2 + \left(bei \sqrt{\sigma} + \frac{\sqrt{2}}{2} \kappa C_\kappa\right)^2},$$

$$B_\kappa = \frac{ber \sqrt{\sigma} + \frac{\sqrt{2}}{2} \kappa D_k}{\left(ber \sqrt{\sigma} + \frac{\sqrt{2}}{2} \kappa D_\kappa\right)^2 + \left(bei \sqrt{\sigma} + \frac{\sqrt{2}}{2} \kappa C_\kappa\right)^2},$$

$$C_\kappa = bei_1 \sqrt{\sigma} - ber_1 \sqrt{\sigma},$$

$$D_\kappa = ber_1 \sqrt{\sigma} + bei_1 \sqrt{\sigma}.$$

The base equation of (13) is identical to that obtained for ideally vented boundary conditions. However, coefficients A_κ and B_κ now contain the pressure flux constriction constant κ. It is readily observed that in the limit of $\kappa = 0$, the original solution obtained by Crandall [1], equation (7), is recovered.

Similarly, the effects of flow constriction on the damping component of the squeeze film may be evaluated by considering the out-of-phase component yielding

$$c_{\text{sf}} = \left\{ -\sqrt{\frac{2}{\sigma}} [A_\kappa (ber_1 \sqrt{\sigma} - bei_1 \sqrt{\sigma}) \right.$$
$$\left. - B_\kappa (ber_1 \sqrt{\sigma} + bei_1 \sqrt{\sigma})] \right\} \frac{P_a A}{d_{\text{gap}} \omega}, \qquad (14)$$

where the coefficients A_κ, B_κ, C_κ and D_κ remain the same as in (13).

2.3.3. Squeeze film constriction. Increasing κ models increasingly restricted flow at the squeeze film boundary. From figure 4(*a*), increasing κ is numerically shown to shift the squeeze film stiffness convergence to lower squeeze numbers and, accordingly, convergence occurs at lower frequencies. The same effect has been shown previously due to specific venting geometries for square plates [12]. In this way, (13) is general and serves as a bridge allowing the characterization of squeeze film behavior not sufficiently described by the limiting cases of equations (4) and (7).

Traditionally, the relative importance of the damping and stiffness in a squeeze film is characterized by the cutoff squeeze number σ_c, which is evaluated where the normalized squeeze film damping and stiffness are equal as shown in figure 4(*a*). Extracted numerically, σ_c decreases exponentially with κ for squeeze numbers up to $\kappa \approx 2.5$, as shown in figure 4(*b*). Using (5), the cutoff frequency ω_c at which the squeeze film stiffness becomes dominate may be estimated using this exponential approximation by

$$\omega_c \approx \frac{P_a d_{\text{gap}}^2}{1.93 \mu_{\text{eff}} R^2} \, \mathrm{e}^{-\kappa} \approx \omega_{co} \, \mathrm{e}^{-\kappa}, \qquad (15)$$

where ω_{co} is the same as that derived analytically by Blech [3] for ideal venting.

The cutoff frequency is rapidly reduced by including the effects of constriction, as shown in figure 5. For example, a structure with a gap aspect ratio R/d_{gap} of 60 would have an ideally vented ($\kappa = 0$) cutoff frequency over 150 kHz, well beyond what may be used in most micromachined accelerometer applications. However, a strongly restricted flow ($\kappa = 2$) results in reducing the cutoff frequency to 20 kHz. In well-vented design, a gap aspect ratio over 160 would be required to achieve such a low cutoff frequency.

2.4. Application to micromachined accelerometers

It has been demonstrated previously that the frequency response of vibratory structures containing a squeeze
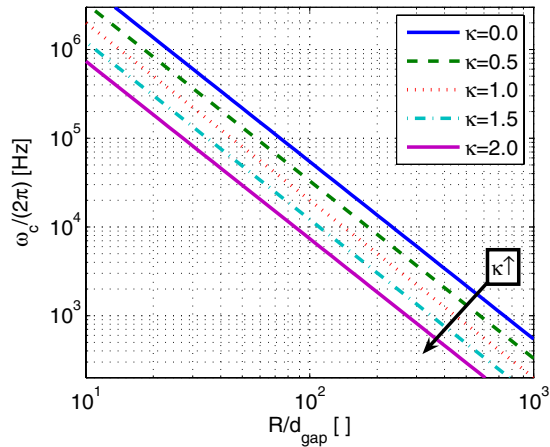
Figure 5. Dependence of the cutoff frequency ω_c on the gap aspect ratio R/d_{gap} for variable constriction κ for a structure of $d_{gap} = 10\ \mu$m at room temperature and atmospheric pressure ($K_n = 0.02$).
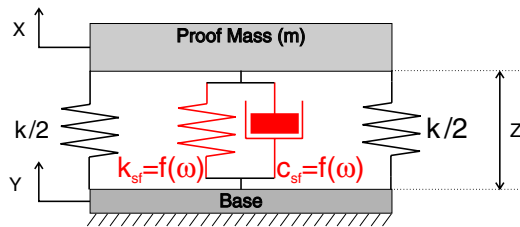

Figure 6. Lumped parameter model with flexure suspension stiffness (k), squeeze film stiffness (k_{sf}) and damping (c_{sf}) under base-displacement excitation Y.

film, such as micromachined accelerometers, are strongly dependent on the value of the cutoff frequency ω_c relative to the natural frequency ω_n of the structure [11]. For devices of $\omega_c \gg \omega_n$ the squeeze film has little effects on the overall response, and for devices of $\omega_c \ll \omega_n$ the low pass sensitivity will degrade significantly due to the increased stiffness in the range from $\omega_c < \omega < \omega_n$. However, where $\omega_c \approx \omega_n$, the squeeze film will introduce a response that extends the vibratory low pass frequency bandwidth without reducing the mechanical sensitivity. Squeeze film constriction in micromachined accelerometers will reduce ω_c to be comparable to ω_n of devices of lower natural frequencies and higher acceleration sensitivities.

2.4.1. Micromachined accelerometer model. A lumped mechanical model may be used to describe the single degree of freedom vibration mode along the sensitive axis, as shown in figure 6. Under base acceleration excitation, the response is given in the Laplace domain as

$$\frac{Z(s)}{A_Y(s)} = \frac{-m}{ms^2 + c_{sf}s + k + k_{sf}}$$
$$= \frac{-1}{s^2 + 2(\omega_n + \omega_{sf})\zeta s + \omega_n^2 + \omega_{sf}^2}, \quad (16)$$

where m is the proof mass, c_{sf} is the damping attributed to the squeeze film and k_{total} is the total structural stiffness composed
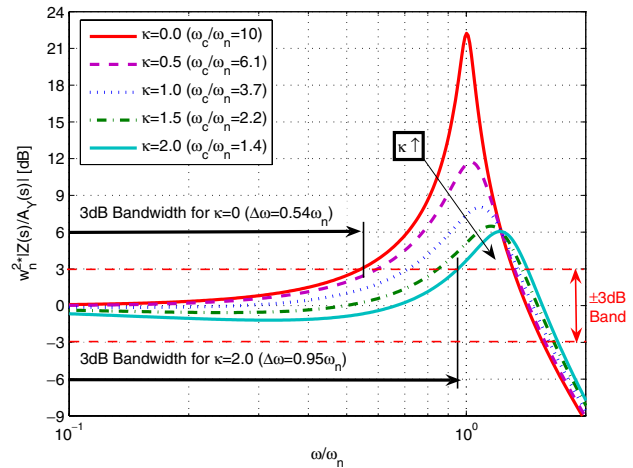

Figure 7. Normalized amplitude frequency response of an accelerometer with constricted squeeze film, where $m = 1$, $k = k_{sf}(\sigma \gg 1) = 1$ and $\omega_{co} = 10\omega_n$.

of the components due to the squeeze film k_{sf} and the flexure suspension k. Normalized by mass, the natural frequency $\omega_n = \sqrt{k/m}$, contribution to the natural frequency due to the squeeze film $\omega_{sf} = \sqrt{k_{sf}/m}$ and damping ratio $\zeta = c_{sf}/2m(\omega_n + \omega_{sf})$ are defined. Assuming small displacements, this linear model with frequency-dependent mechanical parameters may be used to describe the mechanical response of each decoupled mode of a structure with a significant squeeze film, as shown previously by Yang *et al* [7, 8], where the squeeze film parameters c_{sf} and k_{sf} are evaluated at each frequency of interest.

2.4.2. Squeeze film constriction and accelerometer bandwidth. The bandwidth of an accelerometer is defined by the region under which response proportional to acceleration is experienced, which is constrained to the low pass frequency range below resonance and is a fraction of the natural frequency [20].

The response of an accelerometer under varying squeeze film conditions is considered in figure 7. Under ideal venting ($\kappa = 0$), ω_c is defined to be one order of magnitude larger then ω_n. As the constriction is increased, ω_c is reduced such that ω_c approaches ω_n until $\omega_c \approx \omega_n$. This shifts the observed resonant peak at $\omega_n + \omega_{sf}$ to higher frequencies due to the increase in k_{sf}. Since k_{sf} is only appreciable at higher frequencies where the gain has increased due to the resonant response, the bandwidth is increased without a significant decrease in the low frequency gain. The low pass bandwidth for ± 3 dB of magnitude linearity is observed to nearly double to almost equal the natural frequency for a strongly constricted squeeze film ($\kappa = 2$).

2.4.3. Squeeze film constriction and accelerometer sensitivity. The mechanical sensitivity over the low frequency bandwidth is defined as $s \to 0$ in (16) by $|z/a_y| = 1/(\omega_n^2 + \omega_{sf}^2)$. However, it may be assumed that for frequencies below the cutoff frequency, ω_{sf} is negligible. For cutoff frequencies at or above ω_n, the sensitivity is simply $|z/a_y| = (1/\omega_n^2)$ for
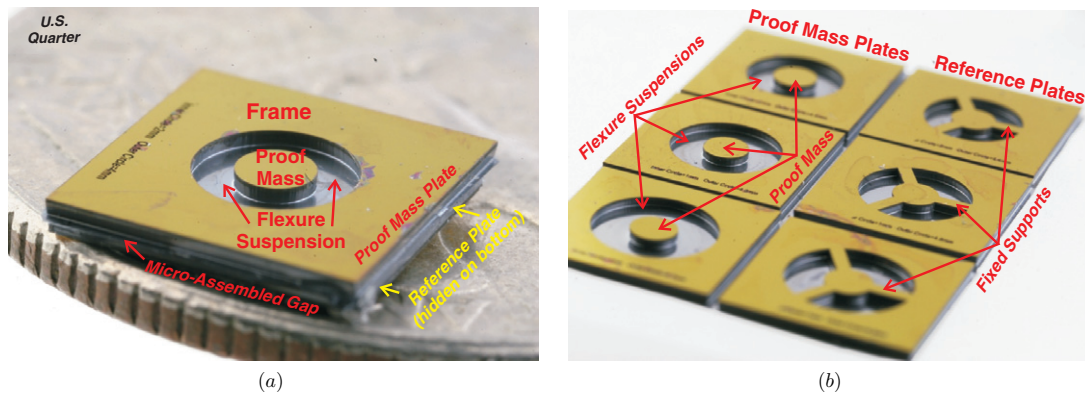
Figure 8. (*a*) A micro-assembled FPI-based inertial sensor (on a US quarter for scale) and (*b*) an array of pairs of micromachined FPI-based inertial sensor components.

$\omega < \omega_c \approx \omega_n$ and the extended bandwidth from the squeeze film is experienced without any loss in sensitivity.

Since increased constriction reduces the cutoff frequency rapidly according to (15), the condition $\omega_c \approx \omega_n$ becomes valid for accelerometers of lower natural frequencies. For moderately constricted geometries ($\kappa = 1$), the 60% reduction under the $\omega_c \approx \omega_n$ condition will result in the bandwidth benefits due to a squeeze film to be present in an accelerometer with five times better sensitivity than an otherwise identical accelerometer with ideal venting ($\kappa = 0$). For more highly constricted geometries ($\kappa = 2$), the reduction in ω_c is better than 85% and better than 40 times increase in sensitivity would be possible over an unconstricted geometry.

3. Characterization

The squeeze film stiffness characteristics of a passive, seismic proof-mass micromachined sensor based on parallel plate Fabry–Pérot interferometers (FPI) are characterized (figure 8(*a*)). The optical characteristics of these devices require geometries that present substantial squeeze film effects, such as large gap aspect ratios and smooth surfaces with no perforations. The devices are formed from pairs of micromachined substrates (figure 8(*b*)) with reflective surfaces micro-assembled to form a gap of parallel faces which are then spaced and fixed. The *proof-mass mirror substrate* is composed of a 'thinned-wafer' flexure connecting the proof mass to a frame fabricated using a simple timed DRIE process. The *reference mirror substrate* contains a similar structure where the flexure has been replaced by fixed supports to minimize compliance. An anti-reflection surface consisting of a single thin film layer silicon nitride is added to the outer surfaces to increase optical transmission through the device. The surfaces of the inner faces of the gap remain polished silicon. Fabrication of the device and a detailed description of the optical and mechanical operation have been presented previously [21, 22].

3.1. Experimental stage

In order to provide swept frequency excitation to the passive FPI-based sensor, a cylindrical piezoelectric stack was inserted

into a vacuum chamber with two collinear optical windows under which the pressure could be varied from below 1 kPa to atmospheric pressure, as shown in figure 9. Two collinear, pigtailed collimated fibers were used as the optical emitter and collectors with laser and broadband sources to allow both static optical and dynamic characterization of the device. When the tunable laser source (HP 8168E) was used, the optical collector was coupled to a photo-collector (Thorlabs PDA255), which provided a voltage signal proportional to the change in optical power δT of the transmitted signal to a dynamic signal analyzer (HP 35665A). The piezoelectric stack excitation voltage was controlled by the dynamic signal analyzer such that during swept sign analysis, the sample response voltage modulation was kept constant to within 1 dB of variation. This ensures that under excitation both (a) the fringe shift $\delta\lambda$ is small in comparison to the fringe width (full-width at half-maximum or FWHM) and the optical properties of $[\delta T/\delta\lambda]_{\lambda_0}$ can be considered as constant and (b) the proof-mass deflection has a constant amplitude of excitation throughout the test. Since the voltage applied to the piezo-stack stage (V_{stage}) is proportional to the base displacement y and the voltage from the photo-collector (V_{FPI}) is proportional to the FPI response due to the proof-mass displacement z, the frequency response can be evaluated by $\left[\frac{Z(s)}{Y(s)}\right] \propto \frac{V_{\text{FPI}}}{V_{\text{Stage}}}$.

3.2. Optical characterization

The gap spacing in the device and the optical transmission spectrum are directly related. This provides the device with both its sensing mechanism and high precision gap characterization not readily available in other micromachined structures. Figure 10 shows the static optical characteristics of the tested sample. From the well-established characteristics of the parallel plate Fabry–Pérot interferometer, the order $n = \lambda_c/\text{FSR} = 21$, the FPI resolution or *finesse* $N = \frac{\text{FSR}}{\text{FWHM}} \simeq 3$, and in air the cavity gap $d_{\text{gap}} = n\lambda_c/2 = 16.5\ \mu\text{m}$ [23]. Thus, the squeeze film gap aspect ratio is $r/d_{\text{gap}} = 60$.

The fringe slope at λ_o at the half-maximum can be characterized directly as from figure 10 and is $[\delta T/\delta\lambda]_{\lambda_0} = 0.05\ \text{nm}^{-1}$. The fringe was limited to shifts of $\simeq 0.2$ nm. From the optical sensitivity of the device and the control voltage, a
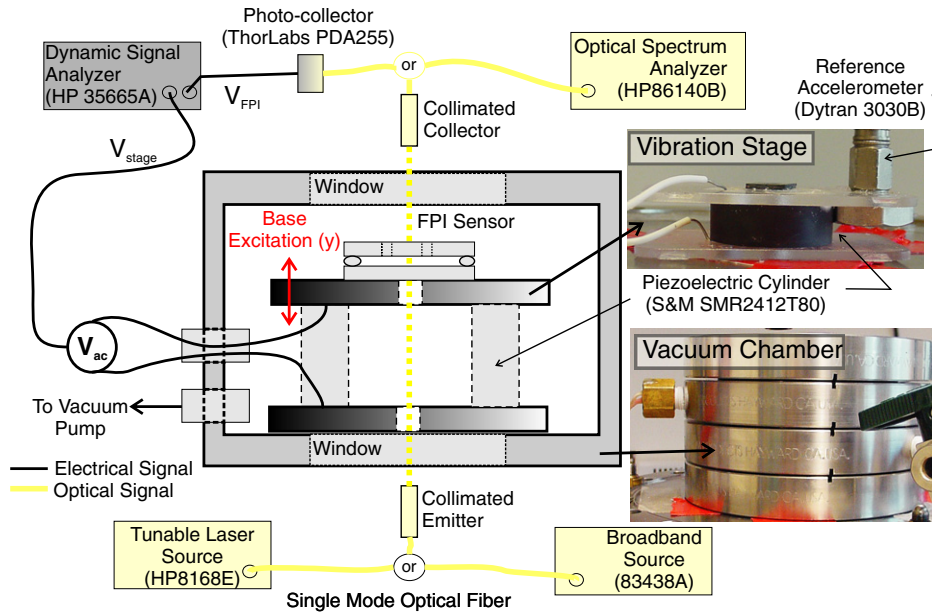
Figure 9. Experimental stage setup for the base excitation of an FPI sensor with pressure variation.
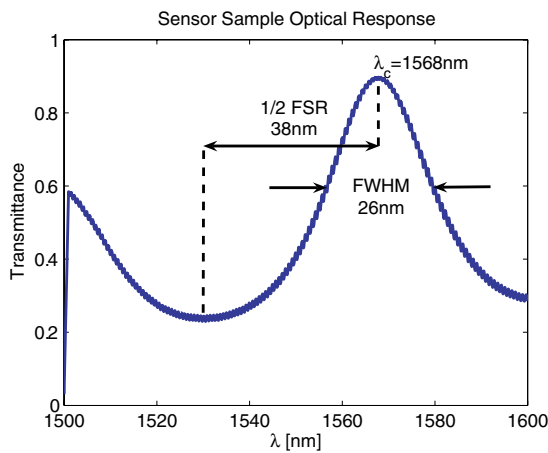

Figure 10. Optical transmission characterization of the sample indicating half the free spectral range (FSR) and full-width at half-maximum (FWHM).

maximum excitation amplitude of ± 22 pm ($\pm 22 \times 10^{-12}$ m) was determined. From the nominal gap spacing at rest, a total deflection of $\simeq \pm 0.1\%$ of the gap was maintained throughout the excitation tests.

3.3. Mechanical characterization

In order to evaluate the mechanical characteristics of the inertial sensor, the frequency response was obtained. Figure 11 shows the frequency response of a device under base-displacement excitation $\left[\frac{Z(s)}{Y(s)}\right]$, resolving both the fundamental first mode and higher second mode. It was shown previously that the fundamental mode is associated with parallel plate normal deflection and may be described by the reduced order model of figure 6(b) and (16), while the higher mode is associated with an out-of-plane angular deflection mode [22].

The phase response of the first mode yields a measure of the total undamped resonate frequency $f_n + f_{sf} = (\omega_n + \omega_{sf})/2\pi$ of the device by calculating the $\pi/2$ phase shift cross-over according to $f_n + f_{sf} = \sqrt{f_{\frac{\pi}{4}} f_{\frac{3\pi}{4}}}$, where $f_{\frac{\pi}{4}}$ and $f_{\frac{3\pi}{4}}$ are the frequencies of $\frac{\pi}{4}$ and $\frac{3\pi}{4}$ phase shift points, respectively [24]. Similarly, the damping ratio is calculated from the phase response according to $\zeta = \left(f_{\frac{3\pi}{4}} - f_{\frac{\pi}{4}}\right) / \left(2\sqrt{f_{\frac{\pi}{4}} f_{\frac{3\pi}{4}}}\right)$ applicable for systems of higher damping ratios. The results are tabulated in table 1 for the low and ambient pressure response. The general shift to higher resonant frequencies as the pressure is increased is indicative of the increasing stiffness due to the squeeze film. Increased damping associated with the squeeze film is noted in response peak broadening with pressure.
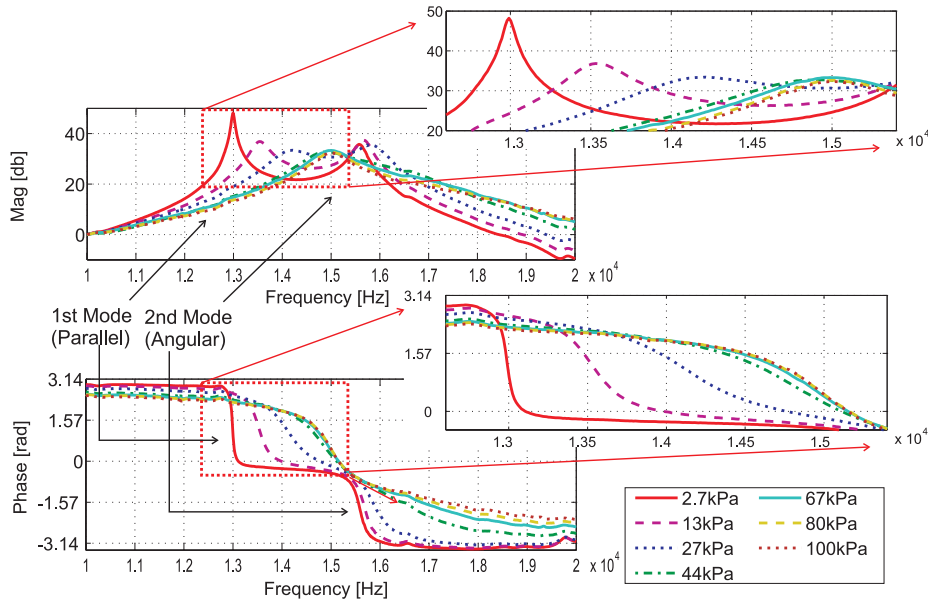
The mass-normalized squeeze film stiffness $\left(\omega_{sf}^2 = k_{sf}/m\right)$ is calculated from the fundamental resonate response according to

$$\frac{k_{sf}}{m} = \omega_n^2 - \frac{k}{m}, \tag{17}$$

where the proof mass m may be readily estimated from the sensor geometry. The normalized flexure stiffness is determined experimentally via $k/m = (2\pi f_n)^2$ from the resonant response under the lowest available pressure. The variation in the normalized squeeze film stiffness is shown in figure 12 versus that predicted analytically by (4), (9) and (13). The squeeze numbers σ are calculated via (5) at the resonance point for each of the frequency sweeps. The pressures during the experiments were selected to provide $K_n < 1$. The expression derived for mixed boundary conditions and non-ideal venting was used to model the response of the device for varying constrictions. A simple graphical analysis allows the parameter κ to be estimated. In this case, the non-ideal venting behavior is reasonably modeled by selecting $\kappa = 1.6$.

Table 1. Properties of the characterized Fabry–Pérot accelerometer.

Geometry See figure 1			Resonant characteristics (figure 11)			
			Reduced pressure (2.7 kPa)		Ambient pressure (100 kPa)	
R	R_o	d_{gap}	f_n	ζ	$f_n + f_{sf}$	ζ
1.0 mm	1.8 mm	16.5 μm	12.9 kHz	0.006	14.5 kHz	0.15

Figure 11. Experimental frequency response of an FPI-based sensor under pressure variation showing the resonant response due to the first and second modes. Inset: detail of the first mode response.
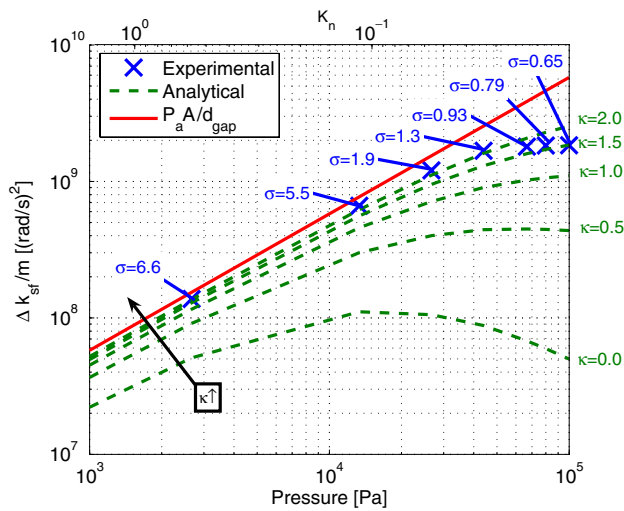
Figure 12. Mass-normalized squeeze film stiffness (k_{sf}/m) extracted through the resonate characterization at the squeeze number σ from figure 11 relative to the Knudsen number K_n and ambient pressure.

One can identify two regions of interest in the response: at lower pressures and higher squeeze numbers, the behavior can be predicted sufficiently by the simplified theory of the compression spring response of (4). At pressures approaching ambient and at lower squeeze numbers, the behavior is more complex. In the ideally vented case ($\kappa = 0$), increasing pressure toward ambient conditions does not necessarily result in an increase in squeeze film stiffness and, at the higher pressures, a large divergence between ideally vented and constricted squeeze film stiffness is observed.

This behavior may be understood by considering the relationship between the cutoff frequency ω_c, vibration frequency ω and squeeze number σ shown in figure 13. At lower pressures the cutoff frequency is well below the structural natural frequency ω_n and the squeeze film stiffness is well described by the simple compression spring. At pressures approaching atmospheric, ω_c becomes greater than ω_n. In this regime, at resonance the stiffness due to the squeeze film is less than the compression spring governed by (7).

It should be noted that at ambient pressures, it is the constriction of the squeeze film that makes this additional stiffness considerable. For ideally venting and $\kappa = 0$, $\omega_c/\omega_n = 11$ and the squeeze film stiffness is negligible. For the experimentally extracted constriction of $\kappa = 1.6$, the cutoff conditions are relaxed and ω_c approaches the natural frequency at atmospheric pressures such that $\omega_c/\omega_n = 2.3$.
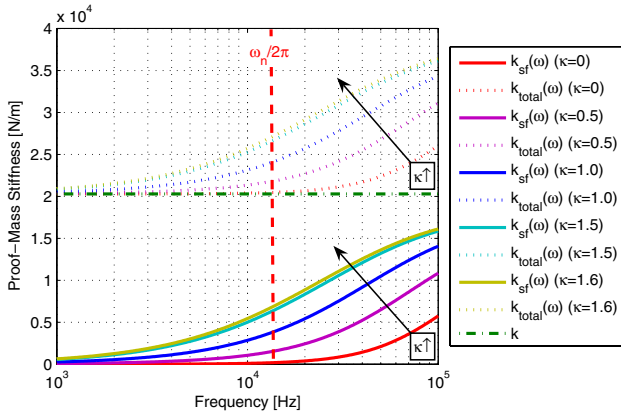
4. Performance

The performance of the sensor characterized in section 3 is now evaluated using the models derived in section 2. Figure 14
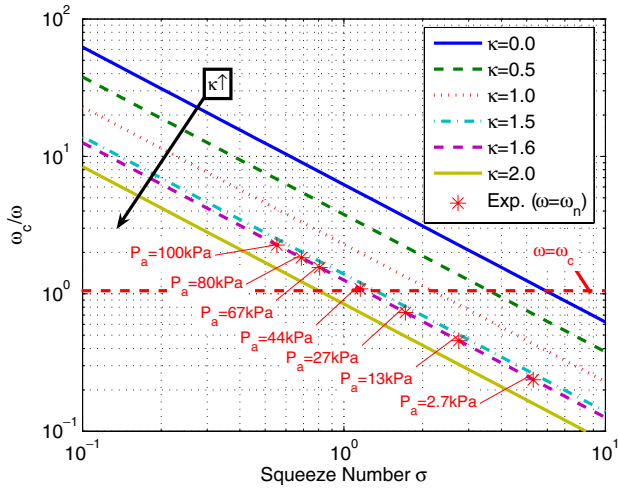
Figure 13. Variation in the fractional cutoff frequency ω_c/ω with squeeze number σ for increasing squeeze film constriction κ. The points where $\omega = \omega_n$ under the experimental pressures are shown for $\kappa = 1.6$ (∗).


Figure 14. Calculated shift in the components and total proof-mass suspension stiffness due to frequency dependence of squeeze films for the experimental characterization shown in figures 11 and 12.

shows the characteristic increase of the proof-mass stiffness with frequency for the experimentally evaluated system with parameters extracted from figure 11 and table 1. The frequency dependence of $k_{\rm sf}(\omega)$ causes the total proof-mass stiffness $k_{\rm total}(\omega) = k + k_{\rm sf}(\omega)$ to rise significantly at frequencies at and above the cutoff frequency ω_c. However, in order to impact the performance of the accelerometer, the increase in total stiffness must be significant when compared to the suspension stiffness k at or below the natural frequency ω_n. By reducing the cutoff frequency, squeeze films of greater constriction cause the stiffness gains from the squeeze film to shift to frequencies falling below the natural frequency ω_n. In this case, constriction as low as $\kappa = 0.5$ is significant enough to elevate the total stiffness observed below the natural frequency.

Figure 15 shows the dynamic response of the evaluated system using the model of (16) with frequency-dependent squeeze film parameters. In addition, the model is evaluated using frequency-invariant parameters extracted experimentally assuming no squeeze film ($k_{\rm total} = k$) and a time-invariant
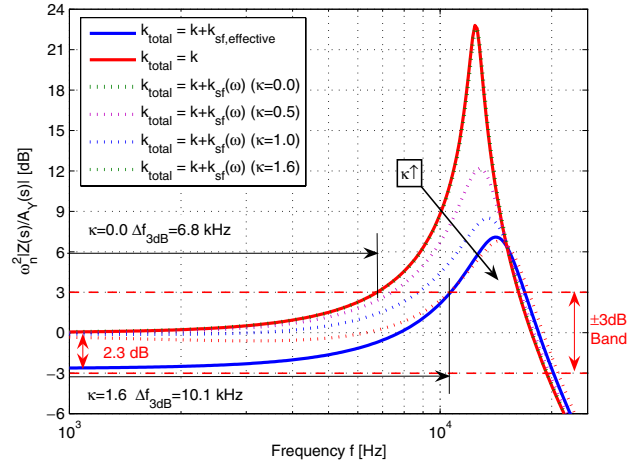
Figure 15. Analytically estimated mechanical response of the accelerometer under the properties calculated from the experimental characterization from figures 11 and 12.
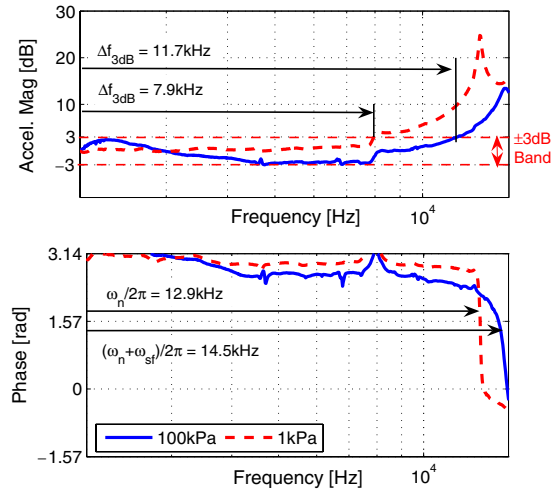
Figure 16. Experimental bandwidth characterization under vacuum ($k_{\rm sf} \approx 0$) and ambient pressures.

equivalent squeeze film stiffness ($k_{\rm total} = k + k_{\rm sf,effective}$) according to table 1. As expected, the increased stiffness due to the squeeze film causes the 3 dB bandwidth to increase significantly, by as much as 3.3 kHz over a system without a squeeze film. It is the venting restriction of $\kappa = 1.6$ that allows these effects to be present. An identical ideally vented squeeze film ($\kappa = 0$) would have negligible effect on the dynamic response of the accelerometer because the stiffness gain is outside the frequencies which define the response of the accelerometer.

Similar bandwidth gains could be achieved through the use of a proof-mass flexure suspension of increased stiffness equivalent to $k_{\rm sf,effective}$. However, such gain would be at the cost of -2.3 dB loss in mechanical sensitivity due to the reduced low frequency gain. Due to the frequency dependence of the stiffness from the squeeze film, the bandwidth gains come without this loss in sensitivity.

Figure 16 shows the experiential bandwidth characterization under both vacuum and ambient conditions over the low

frequency range. The expected bandwidth gain due to the squeeze film is observed from a bandwidth of 7.9 kHz under negligible squeeze film conditions to a bandwidth of 11.7 kHz for the constricted squeeze film, for a total 3.8 kHz gain in bandwidth.

The performance gains from the resonate shift due to a squeeze film may be obtained experimentally from the frequency of the resonant response under the ambient and vacuum conditions, such as the phase crossover frequency shown in figure 16. Since the bandwidth is proportional to ω_n, the fractional bandwidth increase is $|\omega_{n,\text{ambient}}/\omega_{n,\text{vacuum}}|$. This simple analysis yields an estimated 12% gain in bandwidth due to the constricted squeeze film. However, the squeeze film constriction also results in increased damping, which further increases the bandwidth performance. A 48% bandwidth gain is observed both analytically in figure 15 and experimentally in figure 16. Experimentally, up to 91% of the structural natural frequency ω_n may be used with 3 dB of response linearity.

5. Conclusions

This paper characterized the effects of squeeze film constriction on the performance of an optical MEMS accelerometer with a circular proof mass. The constriction of the venting conditions was experimentally shown to result in a shift in the onset of significant stiffness due to the squeeze film. This shift is analytically predicted to occur at lower resonant frequencies under constricted conditions than would otherwise be expected in an accelerometer of an ideally vented geometry. This results in a shift in the resonate response resulting in a gain in sensor bandwidth. A bandwidth gain of over 3 kHz may be attributed to the constriction of the squeeze film in a device with a 12.9 kHz natural frequency resulting in a bandwidth performance gain of 48% achieved without the loss in sensitivity that would be required in a design achieving the same bandwidth without a constricted squeeze film.

Acknowledgments

References

[1] Crandall I B 1918 The air-damped vibrating system: theoretical calibration of the condenser transmitter *Phys. Rev.* **11** 449–60

[2] Langlois W E 1961 Isothermal squeeze films *Q. Appl. Math.* **20** 131–50

[3] Blech J 1982 On isothermal squeeze films *J. Lubr. Technol.* **105** 615–20

[4] Starr J B 1990 Squeeze-film damping in solid-state accelerometers *4th Tech. Digest IEEE Solid State Sensor and Actuator Workshop (Hilton Head Island, SC, 1990)* pp 44–7

[5] Cheng C C and Fang W 2003 Tuning the quality factor of bulk micromachined structures using the squeeze film damping *12th Int. Conf. on TRANSDUCERS, Solid-State Sensors, Actuators and Microsystems* vol 2 pp 1590–3

[6] Pandey A K, Pratap R and Chau F S 2007 Analytical solution of the modified Reynolds equation for squeeze film damping in perforated mems structures *Sensors Actuators* A **135** 839–48

[7] Yang Y J and Senturia S D 1996 Numerical simulation of compressible squeezed-film damping *1996 Solid-State Sensor and Actuator Workshop (Hilton Head, SC)*

[8] Yang Y J, Gretillat M A and Senturia S 1997 Effect of air damping on the dynamics of nonuniform deformations of microstructures *Proc. 9th Int. Conf. on Solid-State Sensors and Actuators (Transducers '97)* vol 2 pp 1093–6

[9] Andrews M, Harris I and Turner G 1991 A comparison of squeeze-film theory with measurements on a microstructure *Sensors Actuators* A **36** 79–87

[10] Veijola T, Kuisma H and Lahdenpera J 1998 The influence of gas–surface interaction on gas-film damping in a silicon accelerometer *Sensors Actuators* A **66** 83–983

[11] Bao M and Yang H 2007 Squeeze film air damping in MEMS *Sensors Actuators* A **136** 3–27

[12] Darling R B, Hivick C and Xu J 1998 Compact analytical modeling of squeeze film damping with arbitrary venting conditions using a Green's function approach *Sensors Actuators* A **70** 32–41

[13] Veijola T, Pursula A and Råback P 2005 Extending the validity of squeezed-film damper models with elongations of surface dimensions *J. Micromech. Microeng.* **15** 1624–36

[14] Minikes A, Bucher I and Avivi G 2005 Damping of a micro-resonator torsion mirror in rarefied gas ambient *J. Micromech. Microeng.* **15** 1762–9

[15] Hutcherson S and Ye W 2004 On the squeeze-film damping of micro-resonators in the free-molecule regime *J. Micromech. Microeng.* **14** 1726–33

[16] Veijola T, Kuisma H, Lahdenpera J and Ryhanen T 1995 Equivalent-circuit model of the squeezed gas film in a silicon accelerometer *Sensors Actuators* A **48** 239–48

[17] Bao M, Yang H, Yin H and Sun Y 2002 Energy transfer model for squeeze-film air damping in low vacuum *J. Micromech. Microeng.* **12** 341–6

[18] Resnick R, Halliday D and Krane K 1992 *Physics* vol 1 (New York: Wiley)

[19] Polyanin A D 2002 *Handbook of Linear Partial Differential Equations for Engineers and Scientists* (London: Chapman and Hall)

[20] Eren H 2000 Acceleration, vibration, and shock measurement *Measurement, Instrumentation and Sensors Handbook* (Boca Raton, FL: CRC Press) chapter 17

[21] Eklund E J and Shkel A M 2005 Factors affecting the performance of micromachined sensors based on Fabry–Perot interferometry *J. Micromech. Microeng.* **15** 1770–6

[22] Perez M A and Shkel A M 2007 Design and demonstration of a bulk micromachined Fabry–Pérot μg-resolution accelerometer *Sensors J. IEEE* **7** 1653–62

[23] Atherton P D, Reay N K, Ring J and Hicks T R 1981 Tunable Fabry–Perot filters *Opt. Eng., Bellingham* **20** 806–14

[24] IEEE 1999 IEEE standard specification format guide and test procedure for linear, single-axis, nongyroscopic accelerometers